EFFECT OF INLET VELOCITY PROFILE AND ENTRANCE LENGTH ON ABDOMINAL AORTIC ANEURYSM HEMODYNAMICS SIMULATIONS

Burcu RAMAZANLI*, Cüneyt SERT**, Mehmet Metin YAVUZ***
*Middle East Technical University, Mechanical Engineering Department
06800, Çankaya, Ankara, karburcu@metu.edu.tr
**Middle East Technical University, Mechanical Engineering Department
06800, Çankaya, Ankara, csert@metu.edu.tr
***Middle East Technical University, Mechanical Engineering Department
06800, Çankaya, Ankara, ymetin@metu.edu.tr

Abstract: In computational Abdominal Aortic Aneurysm (AAA) hemodynamics studies, along with adjusting the problem geometry, mesh, transport, turbulence and rheology models; setting up boundary conditions (BC) is also a very important step which affect the reliability and accuracy of the hemodynamic assessment. The transient effects of physiological flow are well described by the *Womersley* profile, though its application might be difficult due to the complex nature of functions involved. Conversely, in literature, studies utilizing *Plug* or *Parabolic* profiles as inlet boundary conditions generally requires large entrance lengths to obtain the exact characteristics of the *Womersley* profile. In the current study, the differences arising between those boundary conditions, *Womersley*, *Parabolic* and *Plug*, with different entrance lengths, $L_{ent} = D, 3D$ and $11D$, are examined by comparing the results with a Base condition, which is a solution obtained with ensured fully-developed flow before entering the aneurysm sac at two physiological flow conditions with mean Reynolds numbers, $Re_m = 340$ and 1160. The results reveal that with increasing mean flow rate, applying the complex Womersley equation might not be necessary. For the inlet flow waveform with $Re_m = 1160$, the *Parabolic* profile can be used instead of the *Womersley* profile by supplying an entrance length $L_{ent} = 3D$. On the other hand, the *Plug* profile requires an entrance length at least $L_{ent} = 11D$ to replicate the Base condition for waveform with $Re_m = 340$.
Keywords: Abdominal aortic aneurysm hemodynamics, Womersley profile, Wall shear stress parameters, Vortex identification methods

GİRİŞ HIZ PROFİLİ VE GİRİŞ UZUNLUĞUNUN ABDOMİNAL AORT ANEVRİZMASI HEMODİNAMİĞİ SİMÜLASYONLARINA ETKİSİ

Öz: Hesaplamalı Abdominal Aort Anevrizması (AAA) hemodinamiği çalışmalarında problem geometrisi, ağ, taşıma, türbülans ve reoloji modellerinin ayarlanması ile birlikte; sınır koşullarının (BC) belirlenmesi de hemodinamik değerlendirmenin güvenilirliğini ve doğruluğunu etkileyen çok önemli bir adımdır. Fizyolojik akışın geçici etkileri, *Womersley* profili tarafından iyi bir şekilde tarif edilir, ancak ilgili fonksiyonların karmaşık doğası nedeniyle bu profilin uygulanması zor olabilir. Öte yandan, giriş sınır koşulu olarak *Plug* veya *Parabolik* hız profilleri kullanan çalışmalar, *Womersley* profilinin tam özelliklerini elde etmek için genellikle büyük giriş uzunlukları kullanırlar. Bu çalışmada, *Womersley*, *Parabolik* ve *Plug* hız profilleri ve üç ayrı giriş uzunluğu kullanılarak ($L_{ent} = D, 3D$ and $11D$) anevrizma içerisinde hemodinamik parametreler elde edilmiş ve sonuçlar Base koşul ile karşılaştırılarak incelenmiştir. Base koşulu, ortalama Reynolds sayıları $Re_m = 340$ ve 1160 olan iki fizyolojik akış koşulunda, anevrizma içine girmeden önce sağlanan tam gelişmiş akışla elde edilen bir çözümdür. Sonuçlar, ortalama debi arttıkça, karmaşık Womersley denkleminin uygulanmasının gerekli olmayabileceğini ortaya koymaktadır. $Re_m = 1160$ olan giriş debi profili için, en az $L_{ent} = 3D$ olan bir giriş uzunluğu sağlanarak *Womersley* profili yerine *Parabolik* profil kullanılabilir. Öte yandan, $Re_m = 340$ olan debi profil için, *Plug* profilinin *Womersley* profili yerine kullanılması için en az $L_{ent} = 11D$ olan bir giriş uzunluğu gereklidir.
Anahtar Kelimeler: Abdominal aort anevrizması hemodinamiği, Womersley profili, Duvar kayma gerilmesi parametreleri, Girdap tanımlama yöntemleri

NOMENCLATURE

AAA	=	abdominal aortic aneurysm
ILT	=	intraluminal thrombus
WSS	=	wall shear stress [Pa]
$TAWSS$	=	time-averaged wall shear stress [Pa]
$ECAP$	=	endothelial cell activation potential [1/Pa]
OSI	=	oscillatory shear index
L_B	=	bulge length [m]
L_{ent}	=	entrance length [m]
L_{ex}	=	exit length [m]
R_B	=	bulge radius [m]
u_x	=	axial velocity component [m/s]
u_r	=	radial velocity component [m/s]
U_m	=	mean velocity [m/s]
T	=	period of cardiac cycle [s]
ω	=	frequency of cardiac cycle [1/s]
ν	=	kinematic viscosity [m²/s]
Re_m	=	mean Reynolds number $[= U_m D/\nu]$
α	=	Womersley number $[= 0.5D\sqrt{\omega/\nu}]$
τ_w	=	wall shear stress [Pa]
λ_{ci}	=	λ_{ci}-criterion, swirling strength [1/s]
$\overline{\lambda_{ci}}$	=	time – averaged λ_{ci}-criterion [1/s]

INTRODUCTION

Over several decades, intense research on physiologic flow inside the abdominal aortic aneurysms (AAA) have been performed. In order to investigate the hemodynamics inside the abdominal aneurysms, a vast amount of numerical studies is performed (Arzani et al., 2014; Arzani and Shadden, 2016; Drewe et al., 2017; Finol and Amon, 2001). Computational models enable researchers to approximate behavior of blood flow hemodynamics under realistic conditions. The models are generated by defining the conditions on the boundaries and numerically solving governing equations in the fluid domain. Generation of the problem geometry and an appropriate mesh, setting up fluid flow models by adjusting boundary conditions, transport and turbulence properties are important steps which affect the reliability and accuracy of the hemodynamic assessments (Janiga et al., 2015; Salman et al., 2019). Since exact replication of human cardiovascular system is a challenging issue, researchers simplify the problem variables by making different assumptions on their computational models in order to decrease the cost of the solution procedure, which may lead the solutions to be far from the realistic hemodynamics. Indeed, the effect of those assumptions on the solution, and the degree of discrepancy should be examined to guide the researchers during the decision making period of their computational model.

One of the most commonly used assumptions is related to the inlet velocity profile. The most accurate application is utilizing PC-MRI measured patient-specific velocity profiles as an inlet velocity BC, obtained from the human aorta (Chandra et al., 2013;

Youssefi et al., 2018). However, accessing complete high quality patient-specific geometry and inlet profile data is not always possible due to lack of imaging facilities (Armour et al., 2021). Furthermore, directly measuring in vivo inflow conditions is still challenging because of the cardiac motion and resolution (Lodi Rizzini et al., 2020; Markl et al., 2016). Indeed, in several studies it is reported that there is no significant difference between profiles obtained from PC-MRI and artificial ones (Morris et al., 2006; Wei et al., 2019). Therefore, many studies in literature frequently use idealized profiles such as *Plug* (Drewe et al., 2017; Chen et al, 2020), *Parabolic* (Bit et al., 2020; Boyd et al., 2016; Li and Kleinstreuer, 2005; Bilgi and Atalık, 2020) and *Womersley* (Arzani et al., 2014; San and Staples, 2012).

The *Plug* profile is the uniform velocity at the inlet, while the *Parabolic* profile obtained from Poiseuille's equation, and therefore, they cannot present all the characteristics generated due to transitional effects. Although the *Womersley* profile (Womersley, 1955) is necessary to present transient effects especially for large α values, applicability and implementation of the Womersley equation as an inlet boundary condition can be difficult because of the Bessel functions and imaginary numbers that it contains (Campbell et al., 2012; Impiombato et al., 2021). Therefore, in literature, most of the studies utilize *Plug* or *Parabolic* profile with long entrance lengths to obtain fully developed condition (Stamatopoulos et al., 2010), rather than the *Womersley* profile, which increases the computation time. Indeed, the necessary entrance length to obtain fully developed conditions is also a controversial issue. In general, researchers concerned about the inlet velocity boundary conditions and to be on the safe side, they tend to extend the entrance region to ensure fully developed conditions (Madhavan and Kemmerling, 2018). In literature, recommended entrance length values to reach the fully developed state are significantly large (Durst et al., 2005; Salman et al., 2019). On the other hand, Hoi et al. (2010) reported that an entrance length at least three diameters of the artery is sufficient to avoid negligible errors in the hemodynamics of the carotid arteries. However, from a different point of view, Madhavan and Kemmerling (2018) stated that in the actual human arterial system, obtaining the fully developed hemodynamic conditions is not realistic due to the orientation of the vasculature, such as the thoracic aorta is located immediately distal to the heart.

Because the *Womersley* profile resembles the *Parabolic* form at the systole and nearly *Plug* patterns at the diastole (Womersley, 1955), it might be interesting to observe the differences arising from using these three different inlet boundary conditions. In 2012, Campbell et al. hypothesized that the *Womersley* and *Parabolic* inlet velocity boundary conditions give nearly the same result in carotid bifurcation, where $\alpha = 4.1$ and the average radius is 3 mm. However, they highlighted that the results are not applicable for large arteries like the aorta, in

which α is larger than 10, and they require further studies. In 2019, Wei et al. stated that no significant difference between realistic, *Womersley* and *Parabolic* inlet profiles while the *Plug* is notably different that the others for Fontan hemodynamics. However, to the author's best knowledge, there is a deficiency in literature to compare the effect of ideal velocity profiles on abdominal aortic aneurysm hemodynamics, where Womersley number is larger than 10, with different entrance lengths. Also, comparing the profiles at different Reynolds numbers might also be important because the *Womersley* profile shows different patterns for different flow rate values, which can be observed in cardiac conditions such as exercise and rest. Therefore, the aim of the current study is to characterize the behavior of idealized inlet velocity profiles at different entrance lengths and mean flow rates. For that purpose, *Plug*, *Parabolic* and *Womersley* velocity profiles obtained from two mean Reynolds number values, $Re_m = 340$ and 1160, for the same flow waveform pattern for the abdominal aorta are applied as inlet velocity BC to an aneurysm geometry with different entrance lengths, $L_{ent} = $ D, 3D and 11D, where D is the aorta diameter. The results are compared with a fully-developed Base case to check their applicability.

METHODS

The idealized axisymmetric abdominal aortic aneurysm models used in this study are given in Figure 1. Geometries are two dimensional axisymmetric, and created based on those used in Stamatopoulos et. al.'s study (2010). The inlet and exit parts are straight and cylindrical, while the aneurysm bulge is elliptical with a major radius of 0.034 m. The artery and bulge radii are, $R = 9$ mm and $R_B = 22$ mm. The lengths of the bulge and exit part are $L_B = 62$ mm and $L_{ex} = 206$ mm, while entrance lengths, L_{ent}, are different. As presented in Figure 1.b, entrance lengths are equal to $L_{ent} = $ D, 3D, 11D and 50D, from top to bottom and left to right, respectively. At the inlet of the models with $L_{ent} = $ D, 3D and 11D, all the velocity profiles, *Womersley, Parabolic* and *Plug*, are applied. To compare the results obtained with three different entrance lengths and velocity profiles, a Base condition is generated with the model having an entrance length $L_{ent} = $ 50D with only the *Plug* velocity profile at the inlet. The Base condition is checked to ensure the fully developed condition at each time steps before entering the aneurysm sac. In Table 1, the models with applied inlet velocity profiles are also presented. The vessel and bulge dimensions of all models are consistent with realistic arteries and aneurysms (Brewster et al., 2003). Actually, the idealization of the aneurysm bulge rather than utilizing patient-specific geometry may fail to simulate exact aneurysm hemodynamics. However, an idealized axisymmetric geometry is sufficient for a comparative parametric study to compare the behavior of different inlet velocity profiles, which is actually independent of geometric details.

Table 1. Aneurysm models with respect to entrance lengths, L_{ent}, and applied inlet velocity profiles.

L_{ent} (m)	Inlet Velocity Profile	
D, 3D, 11D		Womersley
		Parabolic
		Plug
50D		Plug / **Base Case**

At the inlet, *Womersley*, *Parabolic*, and *Plug* profiles are specified according to the waveform which is considered to be physiologic, as presented in Figure 2a. *Plug* profile is actually the uniform velocity at the inlet, while *Parabolic* and *Womersley* velocity profiles are defined by Eqn. (1) and (2) (Wei et al., 2019, Womersley, 1955), respectively

$$u(r,t) = \frac{2Q(t)}{\pi R^2}\left(1 - \left(\frac{r}{R}\right)^2\right) \tag{1}$$

$$u(r,t) = \frac{2C_0}{\pi R^2}\left(1 - \left(\frac{r}{R}\right)^2\right)$$
$$+ \sum_{n=1}^{N} \frac{C_n}{\pi R^2\left(1 - \frac{2J_1\left(i^{\frac{3}{2}}\alpha_n\right)}{i^{\frac{3}{2}}\alpha_n J_0\left(i^{\frac{3}{2}}\alpha_n\right)}\right)}\left[1 - \frac{J_0\left(\alpha_n\frac{r}{R}i^{3/2}\right)}{J_0(\alpha_n i^{3/2})}\right]e^{i\omega_n t} \tag{2}$$

where α_n is the nth term of Womersley number, ω_n is the nth term of frequency, J_0 and J_1 are the Bessel function of the first kind of order zero and first, respectively (Womersley, 1955). Q is the physiologic flow rate, which is presented in Figure 2a. To obtain the Womersley profile, it is necessary to write the flow rate, $Q(t)$, in the harmonic form as in Eqn. (3)

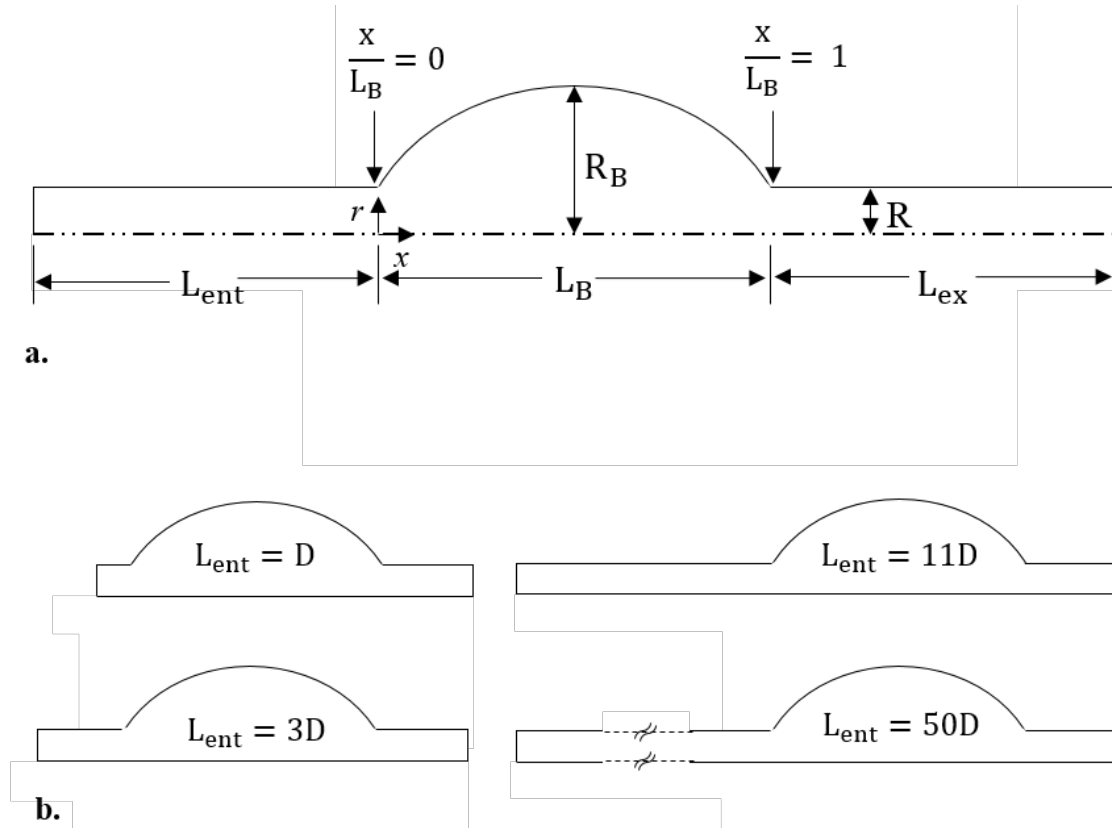$$Q(t) = \sum_{n=0}^{N} C_n e^{i\omega_n t} \tag{3}$$

Figure 1. Sectional views of flow domains for aneurysm models, which is out of scale. Flow is from left to right.

where N is the total number of harmonic coefficients, which is equal to 70 in this study (Wei et al., 2019). A Fourier series decomposition of the flow waveform should be performed to obtain Fourier coefficients, C_n, and Fast Fourier Transforms (FFT) of the flow rates in Figure 2a are used. For that purpose, Fast Fourier Transform (FFT) method is applied to the available flow rate data, as presented in Figure 2a. C_0 and C_n's are the Finite Fourier Transform (FFT) coefficients of that flow rate, while the term n = 0 corresponds to a steady pressure gradient (Wei et al., 2019). Therefore, in Eqn. (2), the first term on the right hand side of the equation is equal to the steady Poiseuille equation (Womersley, 1955), while the second term is obtained from harmonic contribution.

In the current study, simulations are performed at two mean flow rates with Reynolds numbers, $Re_m = U_m D/\nu = 340$ and 1160, based on the mean flow velocity, where $U_m = 0.065$ and 0.22 m/s are the time averaged velocities over one period and $\nu = 3.14 \times 10^{-5} \, m/s^2$ is the kinematic viscosity. The period of all waveform patterns is the same and equal to $T = 1$ s, yielding a Womersley number of $\alpha = 0.5D\sqrt{\omega/\nu} = 12.14$, where D is the artery diameter, ω is the frequency and equals to $2\pi/T$. The waveform pattern for two flows is adapted from the study of Finol and Amon (2001) and is the same for both flow patterns as presented in Figure 2a; however, diastolic flow rate for $Re_m = 1160$ is higher. The reason for using two waveforms is to investigate the effect of increasing mean flow rate on the

applicability of *Parabolic* and *Plug* inlet velocity boundary conditions, rather than the *Womersley* profile. In Figure 2b, Womersley profiles obtained by corresponding waveforms at specified time instants are demonstrated. As can be seen from figure, with increasing flow rate, profiles obtained by Womersley formula are very similar to Parabolic form. The cardiac cycle is divided into six phases, which are early/mid/late systole and diastole. The location of each phase in the cardiac cycle is shown in Figure 2a, while time ranges for these phases are presented in Table 2.

The wall boundaries are taken as rigid and no-slip boundary condition is applied. Excluding the compliance effect with utilizing the walls as rigid is quite common common (Arzani et al., 2014; Finol and Amon, 2001). Reference pressure at the outlet is set to zero, which is a frequently utilized approach in literature for hemodynamics studies (Qiu et al., 2018; Reza and Arzani, 2019). Flow is considered to be laminar (Scotti et al., 2008) due to Reynolds number is not sufficient to reach turbulent conditions even at peak systolic phase, $Re_{peak} = 2000$. In general, blood has non-Newtonian characteristics where the viscosity decreases with increasing shear rate. However, at shear rates higher than $100 \, s^{-1}$, blood shows Newtonian characteristics, and for large arteries, such as the one used in this study, it can be assumed as Newtonian (Reza and Arzani, 2019) with a kinematic viscosity of $3.45 \times 10^{-6} \, m^2/s$, and density of $1000 \, kg/m^3$.
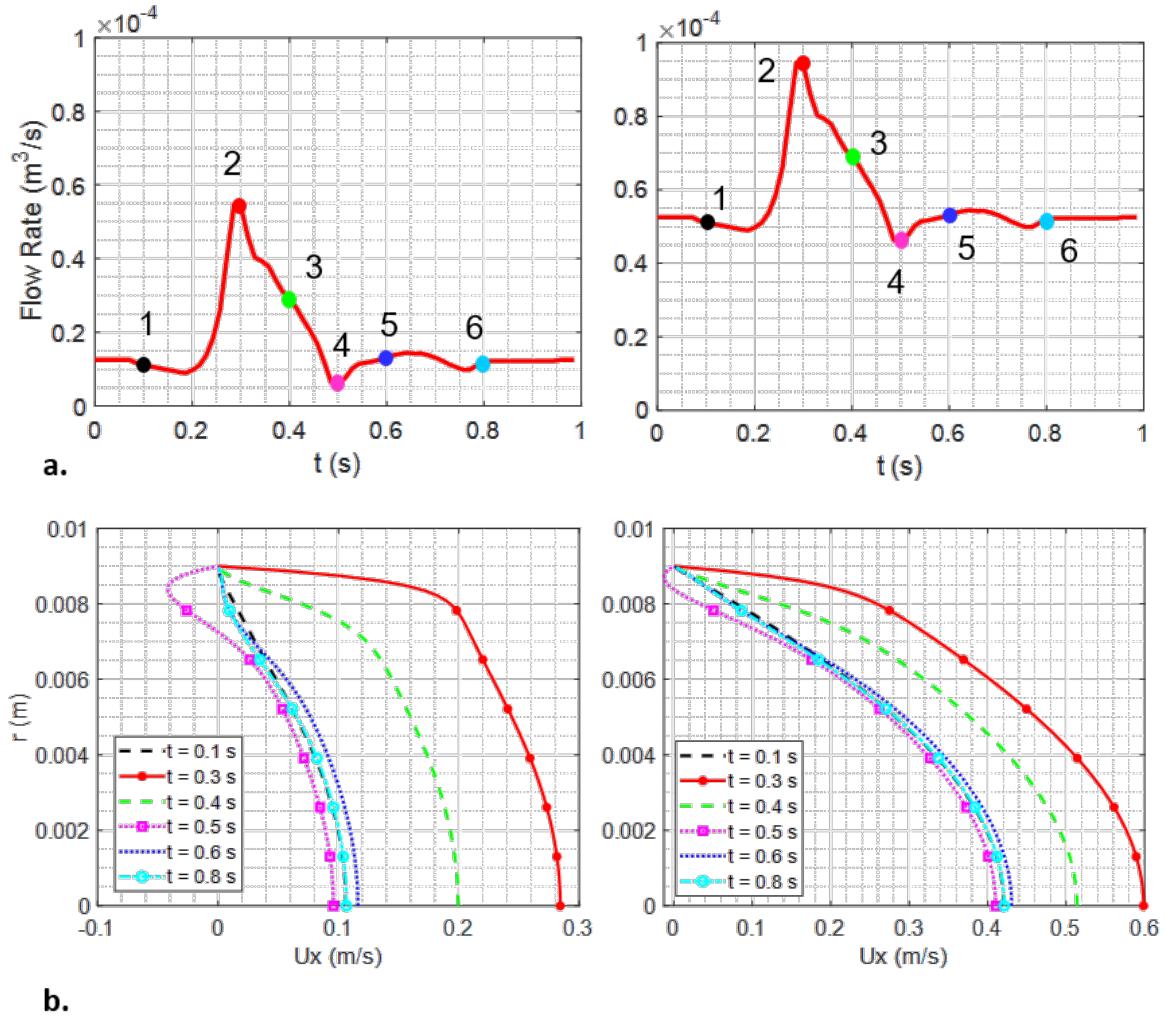
Figure 2. a. Physiological inlet flow rate waveforms and mean Reynolds numbers, $Re_m = 340$ and 1160, from left to right, respectively, with period $T = 1$ s, **b.** Womersley velocity profiles for those waveforms at selected time instants (Finol and Amon, 2001).

Table 2. Phases of cardiac cycle with period T = 1 sec.

Number	Phase	Time interval
1	Late Diastole	0 – 0.18
2	Early Systole	0.18 – 0.3
3	Mid Systole	0.3 – 0.4
4	Late Systole	0.4 – 0.5
5	Early Diastole	0.5 – 0.76
6	Mid Diastole	0.76 - 1

Numerical simulations are conducted by using OpenFOAM version 8 (openfoam.org). The governing equations are discretized using second order implicit discretization in time and second order central discretization in space. pimpleFoam solver is selected because of enabling automatic control of the time step to achieve a given maximum Courant number (C_{max}) for each case. To select an appropriate C_{max} that can provide accurate solutions, five different Courant numbers, which are $C = 0.25, 0.5, 1, 2,$ and 4 were tested, and higher Courant numbers failed to provide stable solutions. For all Courant numbers, the same velocity profile was obtained, meaning that solutions until $C_{max} = 4$ give accurate results for the current study. However, C_{max} was taken as 1 to be on the safe side. 30 iterations are performed at each time step, and the solution is considered to be converged when residuals for axial velocity component and pressure are less than 10^{-4}. To ensure convergence, calculations are repeated for six cardiac cycles.

To select a suitable mesh, a mesh independence study is performed using four structured meshes created, as shown in Fig. 3. Figure 4a shows axial velocity profiles at the mid-plane of the aneurysm and swirling strength, λ_{ci} contours obtained by using these meshes at the peak systole and early diastole. In Figure 4b, OSI and ECAP distributions obtained by those meshes are provided. As from those figures, the axial velocity profiles are identical and swirling strength contours are very similar

for Mesh 3 and 4. Albeit OSI and ECAP distributions are very sensitive to the mesh selection, Mesh 3 and 4 obtain very similar OSI and ECAP distribution. Therefore, Mesh 3 is evaluated to be suitable and used to perform the simulations in the present study.
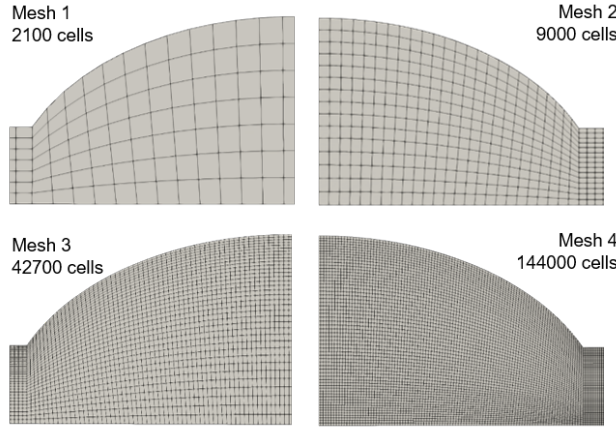

Figure 3. Four meshes generated for mesh independency check.

Stamatopoulos et al. (2010) have performed an experimental and numerical study in axisymmetric bulges similar to the ones used in the current study with a steady inlet flow. In Fig. 5a, axial velocity profiles obtained by Stamatopoulos et al. (2010) are compared with those obtained in the current study with a steady inlet flow. The validation study is performed using the Base case, and the match in the profiles is considered to be satisfactory. Ohtaroglu (2020) performed experiments with physiological, unsteady inlets using Stamatopoulos et al.'s geometry. Figure 5c compares the streamlines obtained in those experiments with the current simulation results at four different time instants of the physiological cycle. Progression of focus points in streamlines which are the indication of vortex core movement shows good agreement. Considering both spatial and the temporal evolution during the cycle, the model predictions are considered to be satisfactory. In addition, simulations are performed to ensure the validity of 2D axisymmetric simplification by comparing results with those of 3D simulations. This simplification aims to decrease the computation time and is justified by performing a sample 3D simulation to see whether there are any 3D effects altering the overall flow structure inside the aneurysm bulge. Considering the velocity profiles plotted at the mid plane of the bulge as demonstrated in Fig. 5c, 2D axisymmetric and 3D results turn out to be almost identical.

WSS Parameters and Swirling Strength

In literature, researchers utilize several physical phenomena to predict aneurysm development, thrombosis formation and rupture. Generally, wall shear stress (WSS) distribution and different WSS descriptors are used for this purpose. TAWSS descriptor evaluates the total shear stress exerted on the wall throughout a cardiac cycle and OSI highlights zones where WSS

shows directional changes over the cardiac cycle (Pinto and Campos, 2016). Mathematical definitions of these descriptors are given below (Salman et al., 2019).

$$TAWSS = \frac{1}{T}\int_0^T |\tau_w|dt \tag{4}$$

$$OSI = 0.5\left(1 - \frac{\left|\frac{1}{T}\int_0^T \tau_w dt\right|}{\frac{1}{T}\int_0^T |\tau_w|dt}\right) \tag{5}$$

$$ECAP = \frac{OSI}{TAWSS} \tag{6}$$

where T and τ_w are the cardiac cycle period and the wall shear stress, respectively.

Inside the aneurysm sac, there is a vortex ring, which evolves throughout the cardiac cycle. λ_{ci}-criterion is a velocity gradient based vortex identification criteria, which uses discriminant of characteristic equation to define a vortex and can be defined as follows (Chen et al., 2015)

$$\lambda_{ci} = \frac{1}{2}\sqrt{-4\frac{\partial u_r}{\partial x}\frac{\partial u_x}{\partial r} - \left(\frac{\partial u_x}{\partial x} - \frac{\partial u_r}{\partial r}\right)^2} \tag{7}$$

where u_r and u_x are radial and axial velocity components, respectively. Around a vortex region, λ_{ci} is larger than zero (Chen et al., 2015).

RESULTS AND DISCUSSIONS

In Figure 6, time-averaged axial velocity profiles obtained with *Womersley*, *Parabolic*, and *Plug* inlet velocity profiles at different entrance lengths for mean Reynolds number, $Re_m = 340$, are presented and compared with the Base condition. The profiles are plotted at proximal, mid, distal and exit sections of the models, where $x/L_B = 0.25, 0.5, 0.75$ and 1. At each section, results obtained with different inlet conditions at different entrance lengths, $L_{ent} = D, 3D,$ and $11D$, are plotted. For each section and entrance length, the time-averaged axial velocity profiles for *Womersley* are the same as in the Base case. For *Parabolic* and *Plug*, the general pattern of time-averaged axial velocity profiles is also very close to *Womersley* and the Base condition for $L_{ent} = 11D$. However, for $L_{ent} = D$ and $3D$, the shape of the time-averaged velocity profiles and maximum velocity values that they obtained are very different from the Base condition. In addition, the backflow region, which is an important characteristic of the aneurysm hemodynamics, is obtained inside the bulge by the *Womersley* and the Base case for all L_{ent} values. Especially for $L_{ent} = D$, *Plug* and *Parabolic* fail to have an accurate backflow region at those sections.
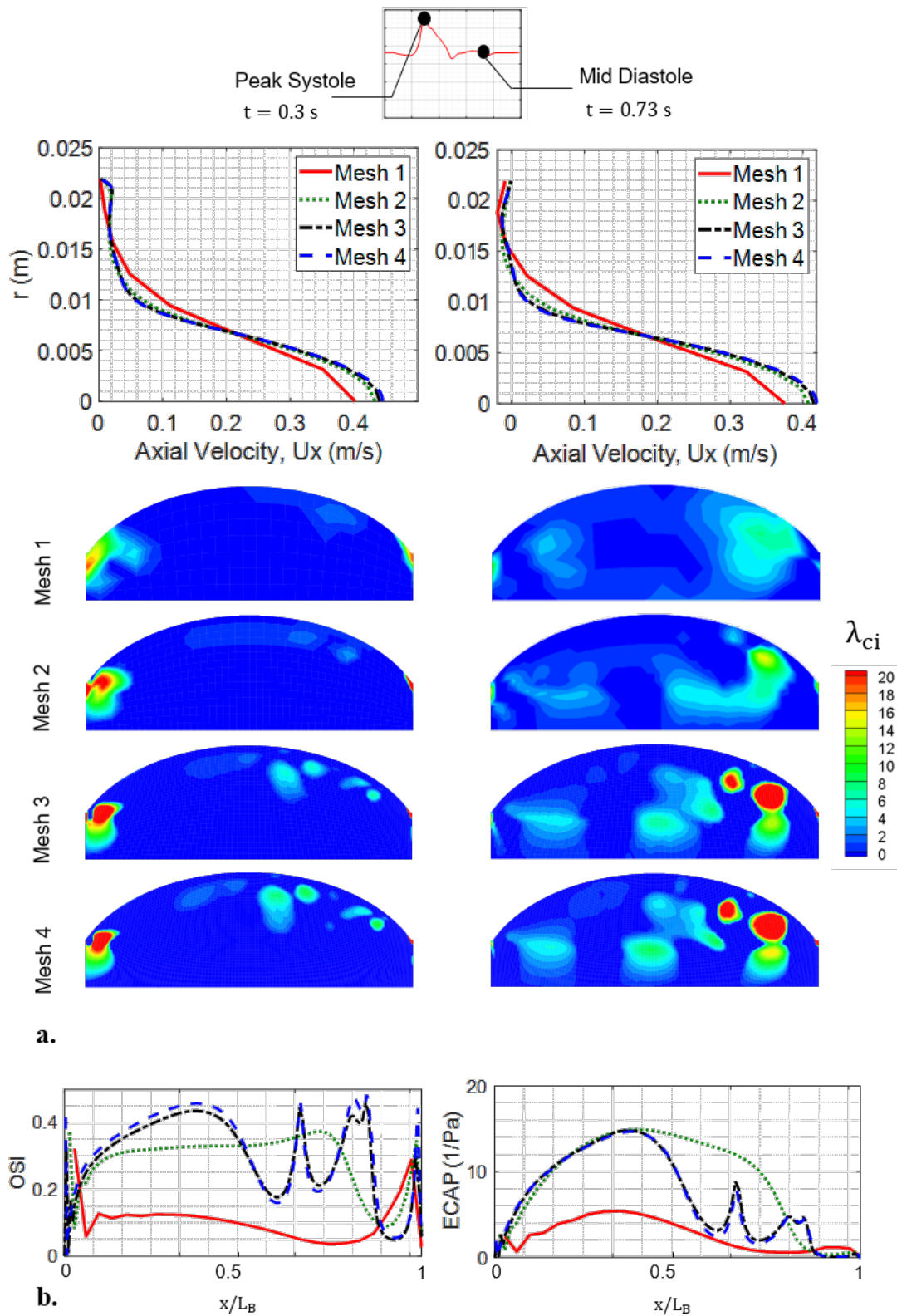
Figure 4. a. Axial velocity profiles, U_x, obtained with four different meshes at the mid-plane of the aneurysm, $x/L_B = 0.5$, and swirling strength (λ_{ci}) contours through the bulge at the peak systole and mid diastole, **b.** OSI and ECAP distributions of four meshes for mean Reynolds number, $Re_m = 1160$.
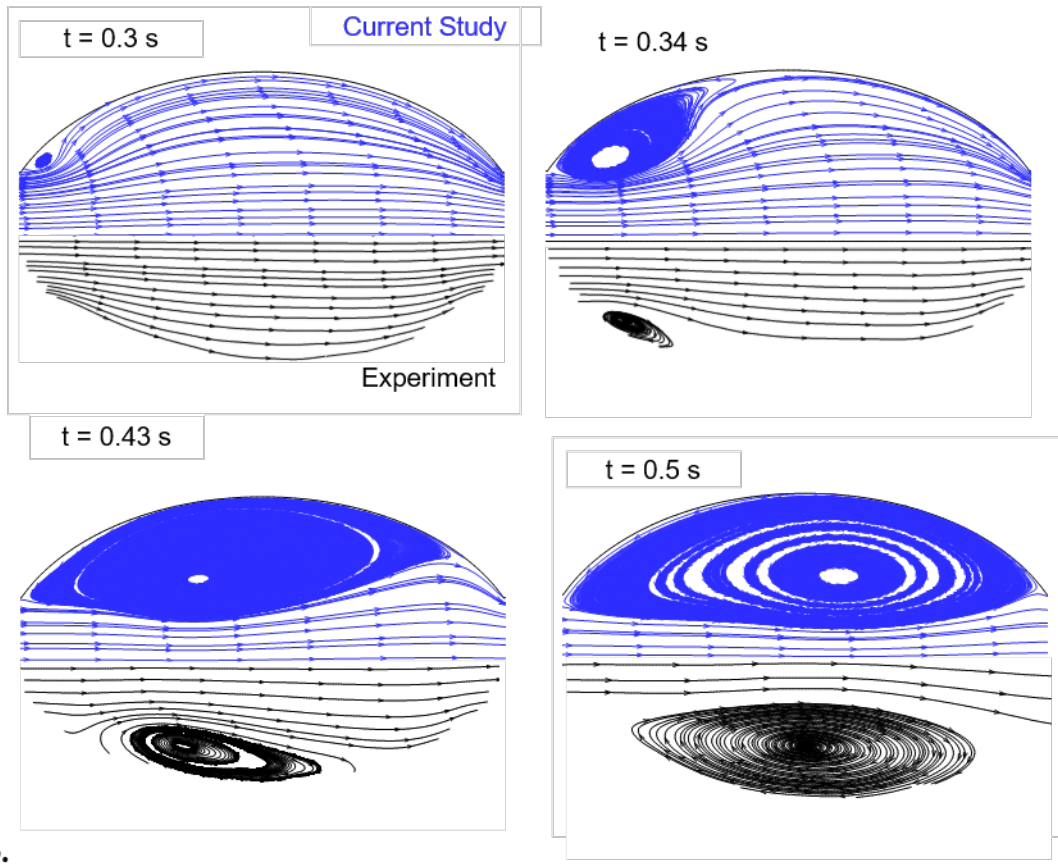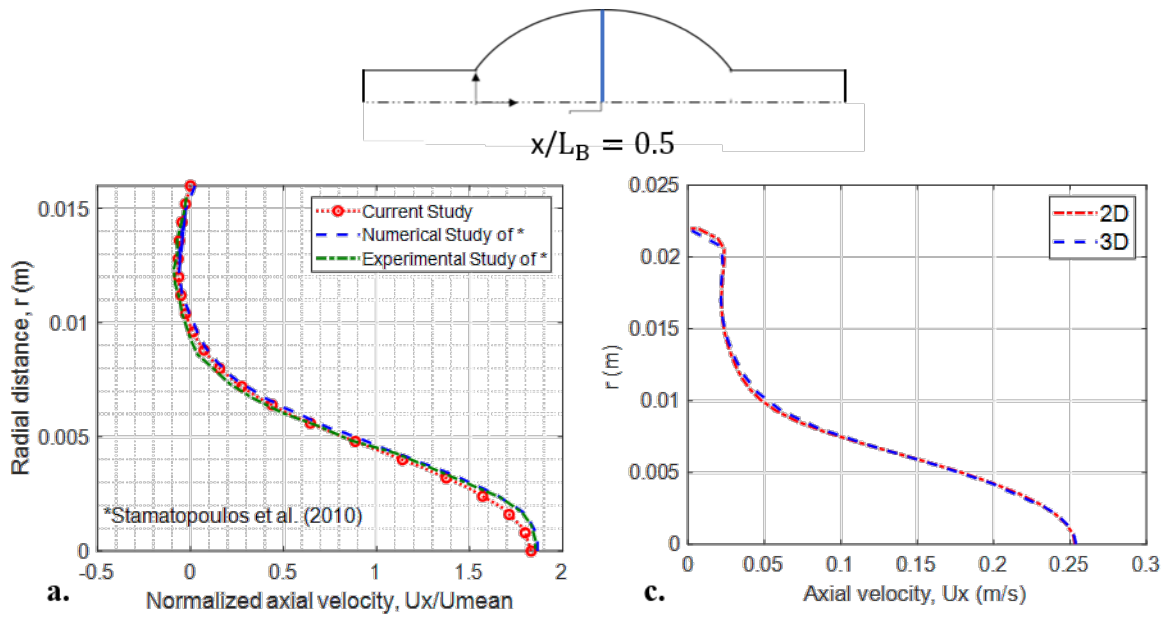
Figure 5. a. Comparison of the normalized axial velocity profile, U_x/U_{mean}, of the current study at the mid-plane of the aneurysm, $x/L_B = 0.5$, with results of Stamatopoulos et al. (2010) for a steady inlet velocity, **b.** Comparison of the streamline patterns of different time instants for a cardiac cycle; upper halves show the current results and lower halves are from Ohtaroglu (2020), **c.** Comparison of the axial velocity profiles, U_x, of 2D axisymmetric and 3D geometries at $x/L_B = 0.5$ at $t = 0.3$ sec.
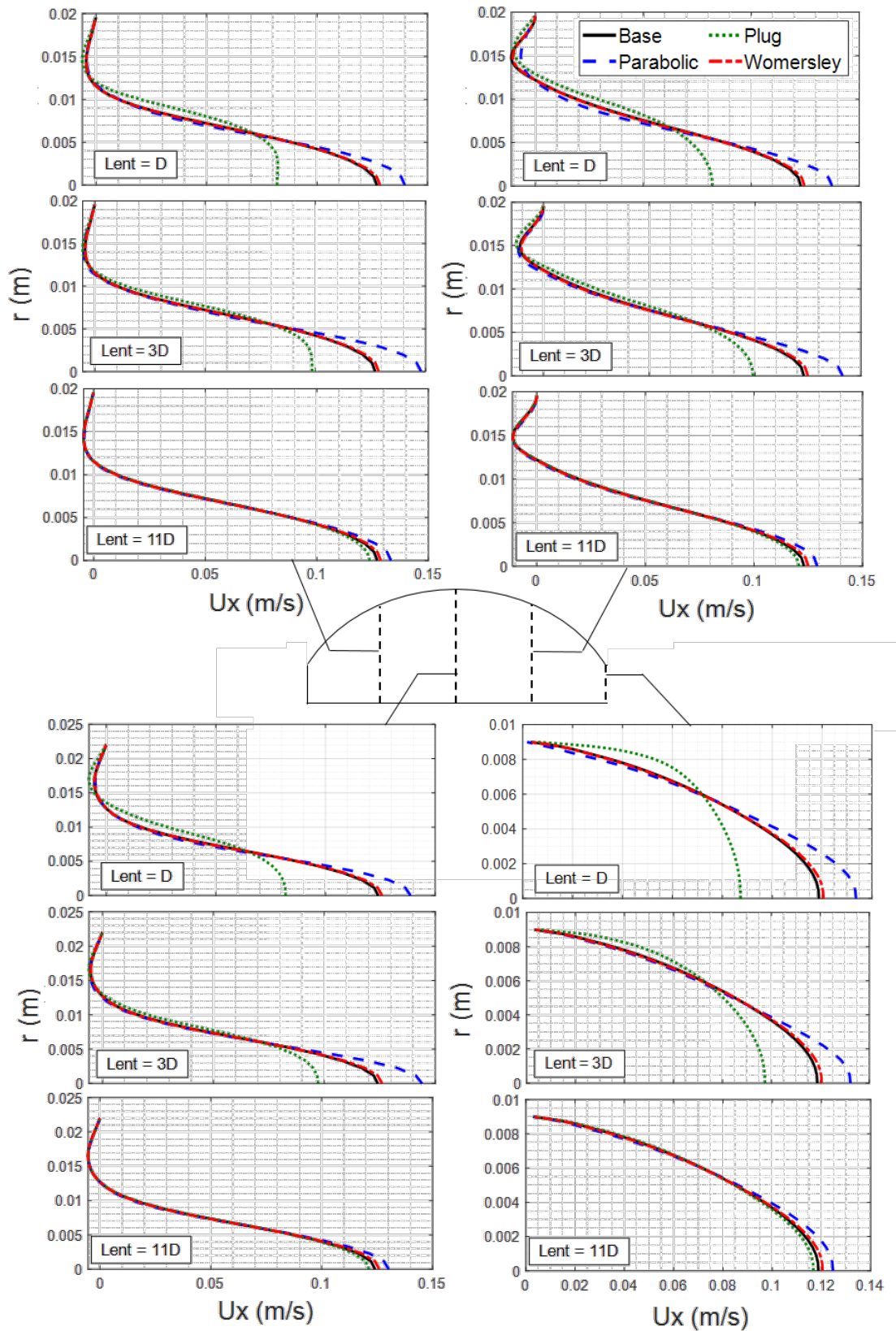
Figure 6. Comparison of time-averaged axial velocity profiles, U_x, obtained by different inlet velocity profiles and entrance lengths for mean Reynolds number, $Re_m = 340$.

Figure 7 shows the time-averaged axial velocity profiles for $Re_m = 1160$ in the same orientation as the Figure 6. For this waveform, similar with the previous case, time-averaged axial velocity profiles for *Womersley* are nearly identical with the Base condition for all entrance lengths. Different from the results for $Re_m = 340$, *Parabolic* also obtains nearly the same velocity profile with *Womersley* and the Base condition for each sections and entrance length, even for $L_{ent} = D$, for $Re_m = 1160$. On the other hand, *Plug* fails to obtain a similar maximum velocity and backflow region with the Base case for both $L_{ent} = D$ and 3D. For $L_{ent} = 11D$, although the maximum velocity value is different, it can capture the backflow region. In addition, time-averaged axial velocity profiles for *Womersley* and *Parabolic* demonstrate a parabolic pattern, while *Plug* has a velocity profile with a flat central part, implying that even $L_{ent} = 11D$ is not sufficient for the *Plug* profile to achieve a fully developed condition for $Re_m = 1160$. For $Re_m = 340$, general pattern obtained by *Plug* is very similar to the *Womersley* and Base condition, while for $Re_m = 1160$, velocity profiles of *Parabolic* are nearly the same with them, even with $L_{ent} = D$. For physiological flows with a high Womersley number, especially $\alpha > 10$, transient inertia forces start to dominate the flow; therefore, velocity profiles resemble plug-like forms with a flattened central profile, and flow reversal areas are also observed due to harmonic contributions coming from transient inertial effects (Womersley, 1955). Indeed, this phenomenon is not governed only by the Womersley number, velocity profiles are also affected by the Reynolds number. For small Reynolds number flows, profiles have a plug-like form with a flattened central profile. With increasing Reynolds number, the effect of steady inertial forces starts to be more dominant, resulting in velocity profiles that are no longer plug-like, but instead more parabolic. Therefore, for $Re_m = 340$, general pattern obtained by *Plug* is very similar to the *Womersley* and Base condition, while for $Re_m = 1160$, velocity profiles of *Parabolic* are exactly the same with them.

In Figures 8 and 9, oscillatory shear index (OSI) and endothelial cell activation potential (ECAP) distributions obtained with *Womersley*, *Parabolic,* and *Plug* inlet velocity profiles at different entrance lengths throughout the aneurysm sac are plotted and compared with the Base case. For $Re_m = 340$ and $L_{ent} = 11D$, OSI and ECAP distributions for all inlet velocity profiles are the same with the Base condition. For $L_{ent} = D$ and 3D, *Womersley* gives the same OSI and ECAP distributions with Base condition. Although the maximum velocity values obtained by *Parabolic* at each section inside the aneurysm are very different for $L_{ent} = 3D$, OSI and ECAP distributions of *Parabolic* are very similar with Base condition because their backflow regions are similar, which affects the WSS parameters considerably. Similarly, for $L_{ent} = D$, in which the backflow region of *Parabolic* and *Plug* are completely different than the Base condition, the WSS parameters are also very

different. For $Re_m = 1160$, *Parabolic* and *Womersley* obtain nearly the same OSI and ECAP distributions with the Base case for $L_{ent} = 3D$ and 11D. Although their results are very similar with each other for $L_{ent} = D$, a deviation from the Base condition is observed. *Plug* fails to provide an accurate OSI and ECAP distribution for $Re_m = 1160$, even with a longer entrance length, $L_{ent} = 11D$.

In Figure 10, for $Re_m = 1160$, instantaneous wall shear stress distributions and contours of swirl strength, λ_{ci}, are presented for late systole and early diastole phases, t = 0.49 and 0.73 sec, through the aneurysm bulge. The top part of the figure shows the results for $L_{ent} = 3D$, while the mid part is for $L_{ent} = 11D$. For the top and mid parts, contours of swirl strength for *Womersley*, *Parabolic* and *Plug* inlet velocity profiles are located, under the instantaneous WSS distributions, from top to bottom, respectively. Contours of λ_{ci} and streamline patterns of the Base condition are located at the bottom part of the figure to compare the results obtained with idealized inlet velocity profiles. From the contours of λ_{ci} for the Base case, at the late systole, t = 0.49 sec, the primary vortex structure is translated to distal end, and a new vortex is originated from the primary vortex structure, which might be labeled as second primary vortex structure. The primary and second primary vortex structures are enclosed by a closed streamline pattern, but they have different vortex cores. At the early diastole, t = 0.73 sec, the primary vortex structure still stays the distal end of the bulge, but its intensity decreases due to viscous diffusion. An additional secondary vortex is generated and located between those two vortex cores, which is very near the wall and has a smaller swirl strength magnitude than the primary vortex.

At each time instant, the contours of swirl strength and instantaneous WSS distributions obtained by *Womersley* and *Parabolic* inlet velocity profiles with $L_{ent} = 11D$ are identical with the Base condition. The vortical structures obtained by *Plug* are also similar in terms of location of cores of the primary vortex structure and the general swirl strength pattern, but the intensity of the contours is significantly different especially in the late systolic and early diastolic phases, for t = 0.49 and 0.73 sec. Also, WSS distributions obtained by the *Plug* case are different than the others at the specified time instants, which is in accordance with swirl strength patterns. For $L_{ent} = 3D$, *Womersley* obtains nearly the same λ_{ci} patterns and WSS distributions as in the Base case. Although the WSS patterns of *Parabolic* are also the same with them, there is a negligible discrepancy in the intensity of the swirl strength contours for t = 0.49 and 0.73 sec. On the other hand, *Plug* obtains completely different results with $L_{ent} = 3D$, which is convenient with the differences observed in time-averaged axial velocity profiles and OSI and ECAP distributions for that inlet condition.
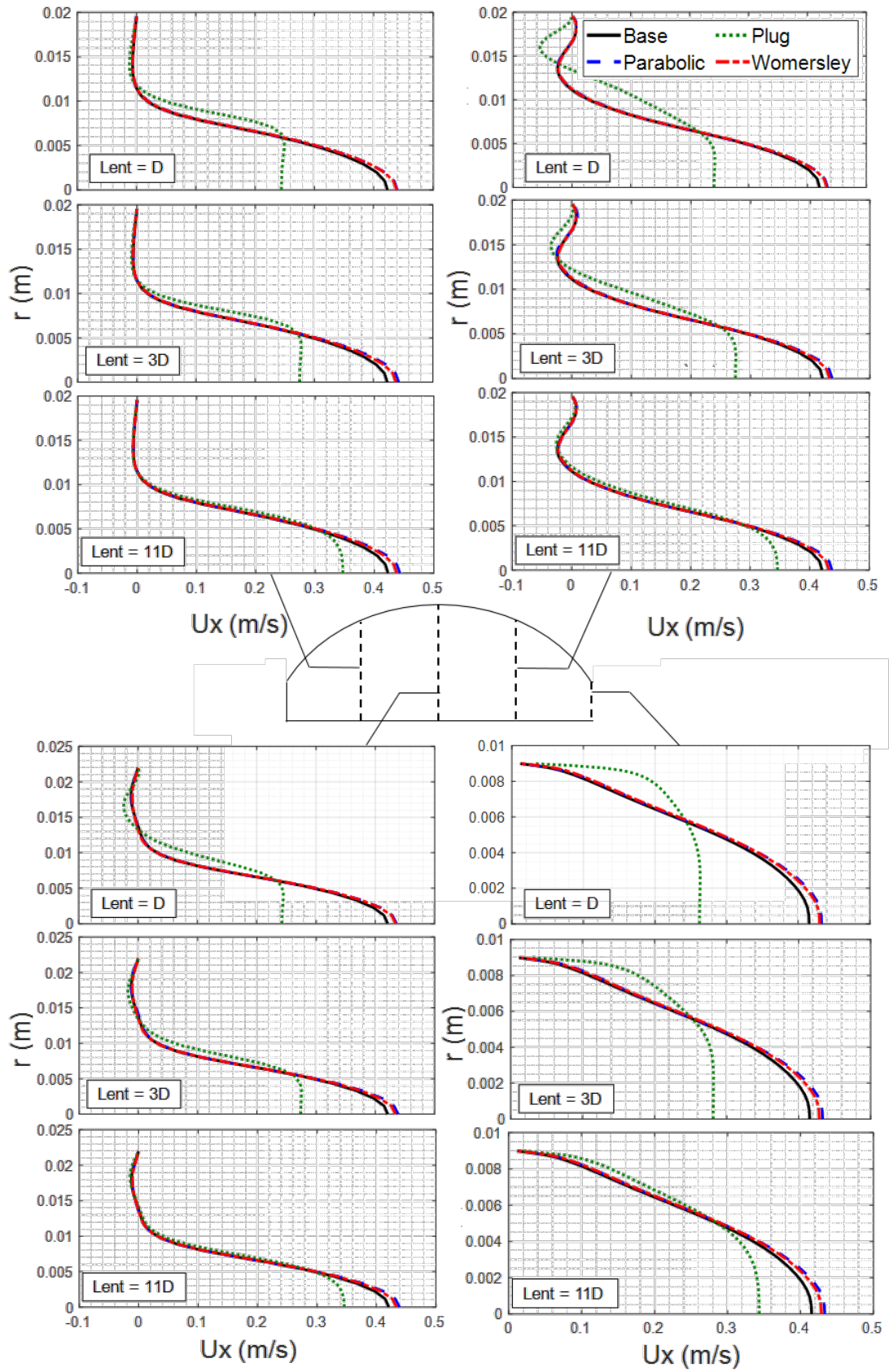
Figure 7. Comparison of time-averaged axial velocity profiles, U_x, obtained by different inlet velocity profiles and entrance lengths for mean Reynolds number, $Re_m = 1160$.
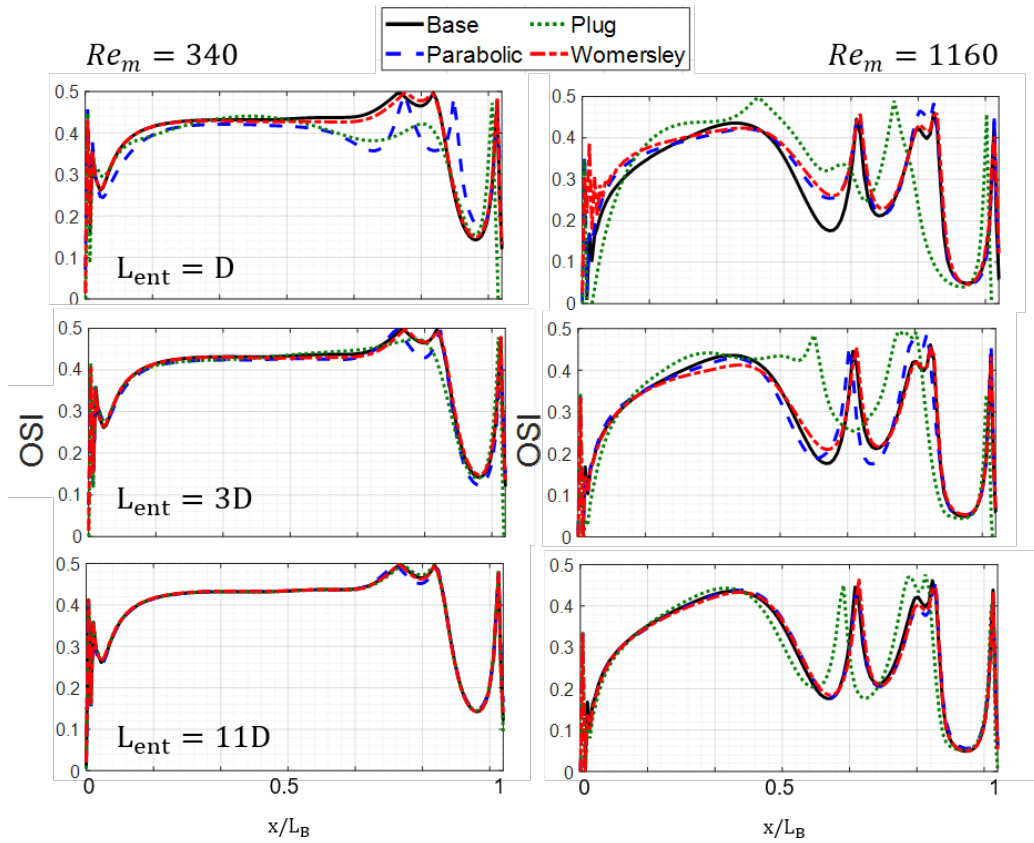
Figure 8. Comparison of oscillatory shear index (OSI) distributions obtained by different inlet velocity profiles and entrance lengths for mean Reynolds numbers, $Re_m = 340$ and 1160, from left to right, respectively.

Figure 9. Comparison of endothelial cell activation potential (ECAP) distributions obtained by different inlet velocity profiles and entrance lengths for mean Reynolds numbers, $Re_m = 340$ and 1160, from left to right, respectively.
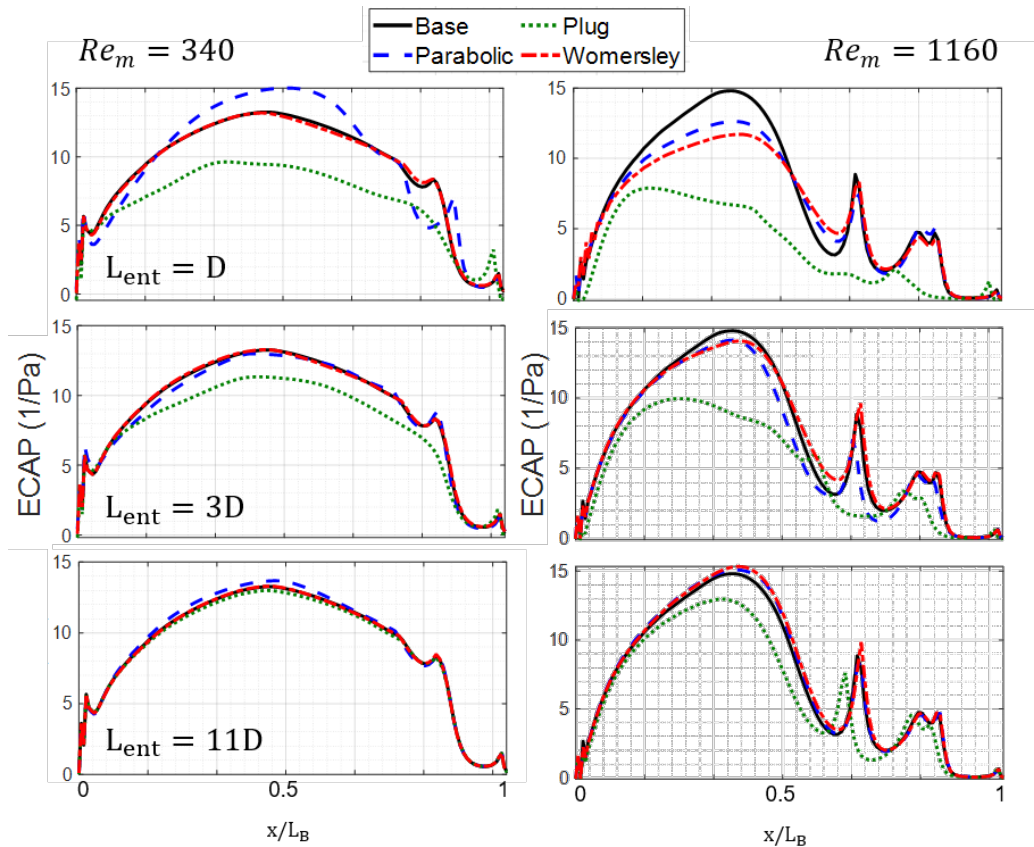
Figure 10. Comparison of instantaneous wall shear stress (WSS) distributions, contours of swirling strength, λ_{ci}, and streamline patterns obtained by different inlet velocity profiles and entrance lengths for mean Reynolds number, $Re_m = 1160$ at t = 0.49 and 0.73 sec.

WSS distributions at different time instants have a correlation with vortex structure movement and swirl strength magnitude, which is also observed by Biasetti et al. (2011). As can be seen in Figure 10, there is a WSS peak around the primary vortex structure which is near the wall at each time instants. With increasing the intensity and magnitude of λ_{ci} of the near-wall vortex structure, the magnitude of the WSS peak also increases. This phenomenon can also be observed in the WSS distribution and λ_{ci} contour of *Plug* at t = 0.49 sec with L_{ent} = 3D. For that time instant, primary vortex structure with a large $|\lambda_{ci}|$ of the *Plug* case is not located in proximity of the wall at the distal area, and its WSS distribution shows a very small peak at that region. Moreover, at t = 0.73 sec, primary vortex structure of *Plug* is not dissipated as much as in the Base condition, and it shows a high swirl strength intensity and WSS magnitude in the distal area, for L_{ent} = 3D. Despite the correlation between the primary vortex structure and WSS magnitude, the second primary vortex structure has no effect on WSS distribution due to the large distance between the vortex and aneurysm wall. However, at t = 0.73 sec, the secondary vortex structure is observed. It has an effect on WSS distribution since it is located in close proximity to the wall. Because the swirling strength magnitude is smaller for the secondary vortex structure, its effect on WSS distribution is also small.

In literature, Wei et al. (2019) have reported that there is no significant difference observed between the realistic, *Womersley*, and *Parabolic* inlet velocity profiles, whereas the *Plug* shows significant variations from the others for Fontan hemodynamics. Moreover, Campbell et al. (2012) have proposed that, in the case of carotid bifurcation with α = 4.1 and an average radius of 3 mm, the *Womersley* and *Parabolic* inlet velocity profiles yield nearly the same results. However, they have emphasized that such findings are not generalizable to larger arteries, such as the aorta, where the value of α exceeds 10, and further investigations are required. In this context, the current study compares the *Womersley*, *Parabolic* and *Plug* profiles for AAA hemodynamics, where the Womersley number is high, α = 12.41. The results demonstrate that, for large mean Reynolds numbers, the hemodynamic parameters obtained by the *Womersley* and *Parabolic* inlet profiles are identical for each entrance length. This might be attributed to the phenomenon that the steady inertial forces become increasingly dominant with increasing Reynolds number, leading to the *Womersley* profile no longer being plug-like and assuming more of a parabolic shape, even for large Womersley numbers. For carotid arteries, Hoi et al. (2010) have reported that an entrance length of L_{ent} = 3D is sufficient to avoid negligible errors. According to the present study, for AAA hemodynamics with a large mean Reynolds number, Re_m = 1160, L_{ent} = 3D might be adequate for the *Womersley* and *Parabolic* profiles to obtain similar results as in the Base case.

CONCLUSIONS

In the current study, the effect of inlet velocity profiles, which are *Womersley*, *Parabolic,* and *Plug*, on predicting hemodynamics by using different entrance lengths is discussed at two different Re_m using the same physiologic flow waveform pattern. Results are compared with the Base condition, which has a very long entrance length with a uniform flow at the inlet to ensure the flow entering the aneurysm sac is fully developed. According to the comparisons of time-averaged axial velocity profiles at different sections inside the sac, OSI and ECAP distributions, instantaneous WSS distributions and swirl strength contours, *Womersley* and *Parabolic* profiles give the same results with Base condition, even with a very small entrance length, L_{ent} = 3D. However, for Re_m = 1160, even the *Womersley* profile could not achieve the same OSI and ECAP distributions as the Base case with L_{ent} = D. With increasing Reynolds number, entrance length requirement of *Womersley* profile becomes nearly the same with *Parabolic* profile. Therefore, especially for high mean flow rates, utilization of *Womersley* profile might not be necessary, which is applicable for the physiological flow waveforms having diastolic flow rates larger than zero. Therefore, rather than applying complex Womersley formulation, utilization of *Parabolic* profile with an entrance length at least L_{ent} = 3D might be appropriate. On the other hand, *Plug* profile cannot obtain similar results with Base condition even L_{ent} = 11D for higher mean flow rates, albeit for R_m = 340, using an entrance length L_{ent} = 11D with *Plug* profile can yield the same results as the Base condition.

The present study, being a comparative parametric analysis, is subject to several limitations that could potentially influence the obtained results. The idealization of aneurysm bulge rather than utilizing patient-specific geometry may lead to inadequate simulation of the exact aneurysm hemodynamics, together with omitting the wall compliance, Windkessel boundary conditions and shear-thinning behavior of actual blood. Therefore, future studies will aim to incorporate patient-specific geometries with elastic walls, along with Windkessel boundary conditions and shear-thinning rheology models to reduce such limitations.

REFERENCES

Armour C. H., Guo B., Pirola, S., Saitta S., Liu Y., Dong Z. and Xu X. Y, 2021, The influence of inlet velocity profile on predicted flow in type B aortic dissection, *Biomech. Model. Mechanobiol.,* 20(2), pp. 481–490, doi: 10.1007/s10237-020-01395-4.

Arzani A., and Shadden S. C., 2015, Characterizations and Correlations of Wall Shear Stress in Aneurysmal Flow, *J. Biomech. Eng.,* 138(1), 014503-014503-014510, doi: 10.1115/1.4032056.

Arzani A., Suh G. Y., Dalman R. L., and Shadden S. C., 2014, A longitudinal comparison of hemodynamics and intraluminal thrombus deposition in abdominal aortic aneurysms, *American Journal of Physiology-Heart and Circulatory Physiology,* 307(12), H1786-H1795, doi: 10.1152/ajpheart.00461.2014.

Biasetti J., Hussain F., and Gasser T. C., 2011, Blood flow and coherent vortices in the normal and aneurysmatic aortas: a fluid dynamical approach to intra-luminal thrombus formation, *J. R. Soc. Interface.,* 8(63), 1449-61, doi: 10.1098/rsif.2011.0041.

Biasetti J., Spazzini P. G., Swedenborg J. and Christian Gasser T., 2012, An integrated fluid-chemical model toward modeling the formation of intra-luminal thrombus in abdominal aortic aneurysms, *Front. Physiol.,* 3, no. July, pp. 1–16, doi: 10.3389/fphys.2012.00266.

Bilgi C. and Atalık K., 2020, Effects of blood viscoelasticity on pulsatile hemodynamics in arterial aneurysms, *J. Nonnewton. Fluid Mech.,* 279, no. July 2019, doi: 10.1016/j.jnnfm.2020.104263.

Bit A., Alblawi A., Chattopadhyay H., Quais Q. A., Benim A. C., Rahimi-Gorji M., and Do H. T, 2020, Three dimensional numerical analysis of hemodynamic of stenosed artery considering realistic outlet boundary conditions, *Comput. Methods Programs Biomed.,* 185, p. 105163, doi: 10.1016/j.cmpb.2019.105163.

Boyd A. J., Kuhn D. C. S., Lozowy R. J. and Kulbisky G. P., 2016, Low wall shear stress predominates at sites of abdominal aortic aneurysm rupture, *J. Vasc. Surg.,* 63(6), pp. 1613–1619, doi: 10.1016/j.jvs.2015.01.040.

Brewster D. C., Cronenwett J. L., Hallett J. W., Johnston K. W., Krupski W. C. and Matsumura J. S., 2003, Guidelines for the treatment of abdominal aortic aneurysms: Report of a subcommittee of the Joint Council of the American Association for Vascular Surgery and Society for Vascular Surgery, *J. Vasc. Surg.,* 37(5), pp. 1106–1117, doi: 10.1067/mva.2003.363.

Campbell I. C., Ries J., Dhawan S. S., Quyyumi A. A., Taylor W. R. and Oshinski J. N., 2012, Effect of inlet velocity profiles on patient-specific computational fluid dynamics simulations of the carotid bifurcation, *J. Biomech. Eng.,* 134(5), pp. 1–8, doi: 10.1115/1.4006681.

Chandra S., Raut S. S., Jana A., Biederman R. W., Doyle M., Muluk S. C., et al., 2013, Fluid-Structure Interaction Modeling of Abdominal Aortic Aneurysms: The Impact of Patient-Specific Inflow Conditions and Fluid/Solid Coupling, *J. Biomech. Eng.,* 135(8), 081001-081001-081014, doi: 10.1115/1.4024275.

Chen X., Zhuang J., and Wu Y., 2020, The effect of Womersley number and particle radius on the accumulation of lipoproteins in the human aorta, *Comput. Methods Biomech. Biomed. Engin.,* 23(10), pp. 571–584, doi: 10.1080/10255842.2020.1752681.

Chen Q., Zhong Q., Qi M. and Wang X. 2015. Comparison of vortex identification criteria for planar velocity fields in wall turbulence, *Phys. Fluids,* 27(8), doi: 10.1063/1.4927647.

Di Achille P., Tellides G., Figueroa C. A., Humphrey J. D., A haemodynamic predictor of intraluminal thrombus formation in abdominal aortic aneurysms, *Proc. R. Soc. A Math. Phys. Eng. Sci.,* 470(2172), 2014, doi: 10.1098/rspa.2014.0163.

Drewe C. J., Parker L. P., Kelsey L. J., Norman P. E., Powell J. T., and Doyle B. J., 2017, Haemodynamics and stresses in abdominal aortic aneurysms: A fluid-structure interaction study into the effect of proximal neck and iliac bifurcation angle, *J. Biomech.,* 60, 150-156, doi: https://doi.org/10.1016/j.jbiomech.2017.06.029.

Durst F., Ray S., Ünsal B., Bayoumi O. A., 2005, The Development Lengths of Laminar Pipe and Channel, *J. Fluids Eng.,* 127, November 2005, 1154–1160, doi: 10.1115/1.2063088.

Finol E. A. and Amon C. H., 2001, Blood flow in abdominal aortic aneurysms: Pulsatile flow hemodynamics, *J. Biomech. Eng.,* 123(5), pp. 474–484, doi: 10.1115/1.1395573.

Hoi Y., Wasserman B. A., Lakatta E. G. and Steinman D. A., 2010, Effect of common carotid artery inlet length on normal carotid bifurcation hemodynamics, *J. Biomech. Eng.,* 132(12), pp. 1–14, doi: 10.1115/1.4002800.

Impiombato A. N., La Civita G., Orlandi F., Franceschini Zinani F. S., Oliveira Rocha L. A. and Biserni, C., 2021, A Simple Transient Poiseuille-Based Approach to Mimic the Womersley Function and to Model Pulsatile Blood Flow, *Dynamics,* 1(1), pp. 9–17, doi: 10.3390/dynamics1010002.

Janiga G., Berg P., Sugiyama S., Kono K., and Steinman D. A., 2015, The computational fluid dynamics rupture challenge 2013 - Phase I: Prediction of rupture status in intracranial aneurysms, *Am. J. Neuroradiol.,* 36(3), pp. 530–536, doi: 10.3174/ajnr.A4157.

Li Z. and Kleinstreuer C., 2005, Blood flow and structure interactions in a stented abdominal aortic aneurysm model, *Med. Eng. Phys.,* 27(5), pp. 369–382, doi: 10.1016/j.medengphy.2004.12.003.

Lodi Rizzini M., Gallo D., De Nisco G., D'ascenzo F., Chiastra C., Bocchino P. P., Piroli F., De Ferrari G. and Morbiducci U., 2020, Does the inflow velocity profile influence physiologically relevant flow patterns in computational hemodynamic models of left anterior descending coronary artery?, *Med. Eng. Phys.,* 82, pp. 58–69, doi: 10.1016/j.medengphy.2020.07.001.

Madhavan S. and Kemmerling E. M. C., 2018, The effect

of inlet and outlet boundary conditions in image-based CFD modeling of aortic flow, *Biomed. Eng. Online,* 17(1), pp. 1–20, doi: 10.1186/s12938-018-0497-1.

Markl M., Schnell S., Wu C., Bollache E., Jarvis K., Barker A. J., Robinson J. D., Rigsby C. K., 2016, Advanced flow MRI: emerging techniques and applications, *Clin Radiol.,* 71(8):779-95, doi: 10.1016/j.crad.2016.01.011.

Morris L., Delassus P., Grace P., Wallis F., Walsh M. and McGloughlin T., 2006, Effects of flat, parabolic and realistic steady flow inlet profiles on idealised and realistic stent graft fits through Abdominal Aortic Aneurysms (AAA), *Med. Eng. Phys.,* 28(1), SPEC. ISS., pp. 19–26, doi: 10.1016/j.medengphy.2005.04.012.

Ohtaroglu O., 2020, Experimental investigation of physiological flow in abdominal aortic aneurysm. METU.

"OpenFOAM 8," OpenFOAM, 01-Sep-2020. [Online]. Available: https://openfoam.org/version/8/. [Accessed: 07-Jun-2022].

Pinto S. I. S. and Campos J. B. L. M., 2016, Numerical study of wall shear stress-based descriptors in the human left coronary artery, *Comput. Methods Biomech. Biomed. Engin.,* 19(13), pp. 1443–1455, doi: 10.1080/10255842.2016.1149575.

Qiu Y., Yuan D., Wen J., Fan Y., and Zheng T., 2018, Numerical identification of the rupture locations in patient-specific abdominal aortic aneurysmsusing hemodynamic parameters, *Comput. Methods Biomech. Biomed. Engin.,* 21(1), 1-12. doi: 10.1080/10255842.2017.1410796.

Reza M. M. S. and Arzani A., 2019, A critical comparison of different residence time measures in aneurysms, *J. Biomech.,* 88:122–9.

Salman H. E., Ramazanli B., Yavuz M. M. and Yalcin H. C., 2019, Biomechanical Investigation of Disturbed Hemodynamics-Induced Tissue Degeneration in Abdominal Aortic Aneurysms Using Computational and Experimental Techniques, *Front. in Biotech and Bioeng.,* 7, no. May, pp. 1–27, doi: 10.3389/fbioe.2019.00111.

San O. and Staples A. E., 2012, An improved model for reduced-order physiological fluid flows, *J. Mech. Med. Biol.,* vol. 12(3), doi: 10.1142/S0219519411004666.

Scotti C. M., Jimenez J., Muluk S. C., and Finol E. A., 2008, Wall stress and flow dynamics in abdominal aortic aneurysms: finite element analysis vs. fluid–structure interaction, *Comput. Methods Biomech. Biomed. Engin.,* 11(3), 301-322. doi: 10.1080/10255840701827412.

Stamatopoulos C., Papaharilaou Y., Mathioulakis D. S., and Katsamouris A., 2010, Steady and unsteady flow within an axisymmetric tube dilatation. *Experimental*

Thermal and Fluid Science, 34(7), 915-927. doi: https://doi.org/10.1016/j.expthermflusci.2010.02.008.

Wei Z.A., Huddleston C., Trusty P.M., Singh-Gryzbon S., Fogel M.A., Veneziani A. and Yoganathan A. P., 2019, Analysis of Inlet Velocity Profiles in Numerical Assessment of Fontan Hemodynamics, *Ann. Biomed. Eng.,* 47(11), pp. 2258–2270, doi: 10.1007/s10439-019-02307-z.

Womersley J. R., 1955, Method for the calculation of velocity, rate of flow and viscous drag in arteries when the pressure gradient is known, *The Journal of Physiology,* 127(3), 553-563. doi: 10.1113/jphysiol.1955.sp005276.

Youssefi P., Gomez A., Arthurs C., Sharma R., Jahangiri, M. and Figueroa C. A., 2018, Impact of patient-specific inflow velocity profile on hemodynamics of the thoracic aorta, *J. Biomech. Eng.,* 140(1), doi: 10.1115/1.4037857.

AUTHORS

Dr. Burcu Ramazanlı*

B.Sc. METU, Mechanical Engineering, 2014
M.Sc. METU, Mechanical Engineering, 2017
Ph.D. METU, Mechanical Engineering, 2022

Prof. Dr. Cüneyt Sert**

B.Sc. METU, Mechanical Engineering, 1996
M.Sc. METU, Mechanical Engineering, 1998
Ph.D. Texas A&M University, Mechanical Engineering, 2003

Prof. Dr. Mehmet Metin Yavuz***

B.Sc. METU, Mechanical Engineering, 2001
M.Sc. Lehigh University, Mechanical Engineering, 2004
Ph.D. Lehigh University, Mechanical Engineering, 2006